



## PLANETARY SCIENCE

# A thermally conductive Martian core and implications for its dynamo cessation

Wen-Pin Hsieh<sup>1,2\*</sup>, Frédéric Deschamps<sup>1\*</sup>, Yi-Chi Tsao<sup>1</sup>, Takashi Yoshino<sup>3</sup>, Jung-Fu Lin<sup>4</sup>

Mars experienced a dynamo process that generated a global magnetic field ~4.3 (or earlier) to 3.6 billion years ago (Ga). The cessation of this dynamo strongly affected Mars' history and is expected to be linked to thermochemical evolution of Mars' iron-rich liquid core, which is strongly influenced by its thermal conductivity. Here, we directly measured thermal conductivities of solid iron-sulfur alloys to pressures relevant to the Martian core and temperatures to 1023 Kelvin. Our results show that a Martian core with 16 weight % sulfur has a thermal conductivity of ~19 to 32 Watt meter<sup>-1</sup> Kelvin<sup>-1</sup> from its top to the center, much higher than previously inferred from electrical resistivity measurements. Our modeled thermal conductivity profile throughout the Martian deep-mantle and core indicates a ~4- to 6-fold discontinuity across the core-mantle boundary. The core's efficient cooling resulting from the depth-dependent, high conductivity diminishes thermal convection and forms thermal stratification, substantially contributing to cessation of Martian dynamo.

## INTRODUCTION

Thermal conductivity of rocky planets' cores controls their thermal evolution and dynamics, which drive and maintain the dynamo action and magnetic fields of these planets (1–3). Convection of an iron (Fe)-rich liquid core is predominantly operated by thermal and compositional buoyancy (4–7). Thermal buoyancy is produced as the super-isentropic heat flux extracted across the core-mantle boundary (CMB) to the mantle is larger than a minimum value. The compositional buoyancy, on the other hand, is generated by a gravitationally unstable density distribution via either phase transition (e.g., crystallization of the liquid core) or exsolution of materials and immiscibility of elements (8–10). The evolution history of the dynamo and magnetic fields of Mars are notably different from those of the Earth: Satellites magnetic data on the Martian crustal rocks suggested an early, short-lived dynamo that once operated ~4.3 (or earlier) to 3.6 billion years ago [Ga; see, e.g., (11–14) for details of the dynamo history], while the Earth's dynamo, predominantly powered by inner core crystallization, remains active today. Paleomagnetic data (15) suggested that Earth's dynamo slowly decayed from 2.5 to 0.5 Ga but recovered as the inner core started to grow. Hemingway and Driscoll (16) suggested that Martian dynamo may be intermittent. They showed that the presence of a solid inner core in Mars is compatible with the absence of a present-day dynamo and that a compositionally powered dynamo could become effective in the next ~1 billion years (Gyr). Moreover, it is worth pointing out that Mercury, which is smaller than Mars but likely to have an inner core with a radius, based on geodetic (17) and magnetic field analysis (18), in the range of ~500 to 660 km, has a faint magnetic field triggered by a core dynamo. However, Venus, whose size is similar to Earth, does not have internal magnetic field at all. These suggest that the size of a planet is not the primary parameter controlling the presence of dynamo and that other aspects, including core

composition and its effects on physical properties, play crucial roles in maintaining a dynamo. Martian core's thermal conductivity holds a key to estimate the available thermal and compositional energy to operate its dynamo and thus to reconstruct its thermochemical history. Recent numerical simulations (1) explored the influence of thermal conductivity on core evolution by doing a systematic parameter survey over a broad range of potential thermal conductivity values and revealed that a high core thermal conductivity (16 to 35 W m<sup>-1</sup> K<sup>-1</sup>) could be a critical factor to cease its global magnetic field. The assumption that thermal conductivity at Martian core's condition is high has, however, never been experimentally verified.

Recent seismic observations by the InSight lander (19, 20) suggested that the Martian core has a radius in the range of ~1620 to 1700 km and is surrounded by a molten layer of silicate rocks of about 150 km thick. Furthermore, it is implied that the entire Martian mantle has a mineralogy similar to that in the Earth's upper mantle and transition zone, i.e., ringwoodite is the major mineral in Martian deep mantle, while bridgmanite, the predominant mineral in Earth's lower mantle, is not present within Mars. Given the limited cosmochemical and geophysical data as well as different model assumptions, the composition of the Martian core remains poorly constrained [see (19–23) and references therein]. However, it is commonly considered to be made of Fe alloyed with significant amounts of light elements, including sulfur (S) as the major one, along with small amounts of oxygen (O), carbon (C), and hydrogen (H). Because of the abundance and siderophile characteristic of S, its proposed content in the Martian core typically falls in the range of ~10 to 25 wt % (22–24). This motivates us to choose, for simplicity, eutectic Fe<sub>3</sub>S (~16 wt %) and FeS (~36 wt %) as representative compositions and to study their thermal conductivity at Martian core pressure-temperature (*P-T*) conditions, providing pivotal insights to their impacts on the fate of Martian dynamo.

The heat flux across the Martian CMB,  $Q_c$ , is crucial for determining the evolution of the thermal state and dynamo action in the Martian core. This flux is controlled by heat transfer through the mantle, which itself depends on the lowermost mantle thermal conductivity, as it controls the conductive heat transfer through thermal boundary layers, as well as on the efficiency of mantle convection (if happening at all). The lowermost mantle thermal conductivity may

<sup>1</sup>Institute of Earth Sciences, Academia Sinica, Taipei 11529, Taiwan. <sup>2</sup>Department of Geosciences, National Taiwan University, Taipei 10617, Taiwan. <sup>3</sup>Institute for Planetary Materials, Okayama University, Misasa 682-0193, Japan. <sup>4</sup>Department of Geological Sciences, Jackson School of Geosciences, University of Texas at Austin, Austin, TX 78712-0254, USA.

\*Corresponding author. Email: wphsieh@earth.sinica.edu.tw (W.P.H.); frederic@earth.sinica.edu.tw (F.D.)

Copyright © 2024 the Authors, some rights reserved; exclusive licensee American Association for the Advancement of Science. No claim to original U.S. Government Works. Distributed under a Creative Commons Attribution NonCommercial License 4.0 (CC BY-NC).

be estimated from mineral physics measurements of ringwoodite's thermal conductivity (25). On the core side, heat transfer and dissipation, which play a crucial role on the core and dynamo evolutions, depend on the core's thermal conductivity. The thermal conductivity of Fe-S alloys may bring important constraints on this conductivity but has never been directly measured under Martian core's high  $P$ - $T$  conditions. Previous studies have largely focused on the determination of the electrical resistivity  $\rho$  of Fe-S alloys, which is then used to infer its thermal conductivity through the Wiedemann-Franz (WF) law with ideal Lorenz number [see, e.g., (26) and references therein]. First-principles theoretical calculations showed that at Martian core conditions the  $\rho$  of liquid  $\text{Fe}_3\text{S}$  and  $\text{Fe}_7\text{S}$  remains at  $\sim 107$  and  $\sim 88$  microhm cm, respectively (27); these results infer a relatively high Martian core's thermal conductivity ( $\sim 50 \text{ W m}^{-1} \text{ K}^{-1}$ ). Note that with similar approaches, Earth's core thermal conductivity was inferred to be  $\sim 80$  to  $300 \text{ W m}^{-1} \text{ K}^{-1}$  (26). Experimental high  $P$ - $T$  measurements on the  $\rho$  of solid Fe-S alloys were, however, typically limited to  $\leq 10$  GPa (28–30). Extrapolation of such low-pressure data to Martian core's high-pressure conditions ( $\sim 18$  to  $40$  GPa) suggested a low thermal conductivity of  $\sim 10 \text{ W m}^{-1} \text{ K}^{-1}$  in Martian core. These contradictory results lead to distinct implications for the energy budget of the Martian core and  $Q_c$  and different scenarios for the evolution of the dynamo. Since the validity of applying the WF law with ideal Lorenz number on the Fe-light element alloys (e.g., Fe-S alloys) under extreme conditions remains uncertain and is being challenged (2), direct and precise determination of their thermal conductivity at high  $P$ - $T$  conditions relevant to the Martian core is key to constrain its thermal conductivity and understand the mechanisms that stop its dynamo.

In this work, our direct high  $P$ - $T$  thermal conductivity measurements of Fe-S alloys combined with data modeling allow us to build a depth-dependent thermal conductivity profile from the Martian deep-mantle to its core, providing the first direct experimental evidence for a highly thermally conductive Martian core. Such high thermal conductivity enables efficient cooling of the Martian core and formation of thermal stratification layer, leading to a short-lived ( $\sim 0.5$  to  $0.8$  Gyr) dynamo that ceased  $\sim 4$  Ga.

## RESULTS

### Thermal conductivity at high pressure and room temperature

We used time-domain thermoreflectance (TDTR) coupled with diamond anvil cell (DAC) (2, 31, 32) (see Materials and Methods) to precisely measure the thermal conductivity of polycrystalline  $\text{Fe}_3\text{S}$  and FeS to  $\sim 40$  GPa at room temperature. (Although measurements on these materials in liquid phase at high  $P$ - $T$  are more relevant to Mars' liquid core, now, they are technically challenging; we thus performed measurements to provide reliable thermal conductivity values of these solid Fe-S alloys at high  $P$ - $T$  and then extrapolated the results into their liquid phase by considering the melting effect on conductivity, see below.) We find that the thermal conductivity of  $\text{Fe}_3\text{S}$  ( $\sim 16$  wt % S) at ambient conditions is  $\sim 6.8 \text{ W m}^{-1} \text{ K}^{-1}$  (Fig. 1A), which is more than an order of magnitude smaller than that of pure Fe ( $\sim 76 \text{ W m}^{-1} \text{ K}^{-1}$ ) (2), indicating a strong reduction of thermal conductivity caused by the sulfur impurity. Application of pressure monotonically enhances the thermal conductivity, which reaches  $\sim 25 \text{ W m}^{-1} \text{ K}^{-1}$  at  $40.5$  GPa, the pressure at the center of the Mars. Moreover, with  $\sim 36$  wt % S impurity, the FeS shows drastically

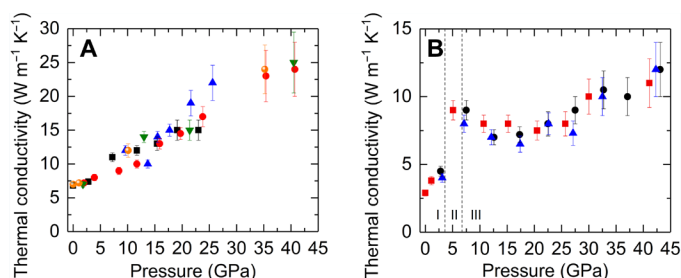


**Fig. 1. Thermal conductivity of Fe-S alloys at high pressure and room temperature.** For both (A)  $\text{Fe}_3\text{S}$  and (B) FeS compositions, several runs of measurements show consistent results, where each run is represented by a symbol set. Vertical bars show uncertainties, which are mainly from the error propagations in spectral modeling analysis:  $<10\%$  before 20 GPa and  $\sim 10$  to  $17\%$  at 20 to 40 GPa. Note that at  $\sim 40$  GPa, the thermal conductivity of FeS is only half of the  $\text{Fe}_3\text{S}$ , indicating a strong reduction by the sulfur impurity. For FeS in (B), the two vertical dashed lines represent the phase transition pressures for FeS I to II at  $\sim 3.4$  GPa and II to III at  $\sim 6.7$  GPa (38). The pressure uncertainty is typically  $\sim 0.1$  to 1 GPa.

distinct values of thermal conductivity and pressure dependence (Fig. 1B). The thermal conductivity of FeS at ambient conditions (FeS I phase) is even lower than that of  $\text{Fe}_3\text{S}$ , down to  $\sim 2.9 \text{ W m}^{-1} \text{ K}^{-1}$ . Upon compression across  $\sim 3.4$  GPa, the thermal conductivity suddenly increases to  $9 \text{ W m}^{-1} \text{ K}^{-1}$  at  $5.2$  GPa (FeS II phase). After the transition at  $\sim 6.7$  GPa to FeS III phase, considering the data uncertainty, the thermal conductivity remains approximately at  $7.5 \text{ W m}^{-1} \text{ K}^{-1}$  until  $\sim 25$  GPa, after which it significantly increases to  $12 \text{ W m}^{-1} \text{ K}^{-1}$  at  $43$  GPa, half of the  $\text{Fe}_3\text{S}$  at similar pressures.

It is worth noting that, similar to the effect of silicon alloying (2), the presence of  $\sim 16$  wt % ( $\text{Fe}_3\text{S}$ ) and  $\sim 36$  wt % S (FeS) in Fe significantly reduces the thermal conductivity, presumably due to the strong inelastic scattering between electrons and impurities (33–35). The impurity effects also alter the pressure dependences of  $\text{Fe}_3\text{S}$  and FeS, which are considerably different from that of pure Fe, where a concave pressure dependence with a minimum at  $\sim 40$  GPa was observed (2).

### Thermal conductivity at high pressure-temperature conditions

To quantify the effects of temperature and sulfur alloying, we further performed high  $P$ - $T$  thermal conductivity measurements on the  $\text{Fe}_3\text{S}$  and FeS in externally heated DACs (EHDACs; Fig. 2). The thermal conductivities of  $\text{Fe}_3\text{S}$  and FeS both increase with temperature, similar, again, to the behaviors of Fe-Si alloys (2, 36). Note that along the  $P$ - $T$  path of our measurements (i.e., first compressing the sample to a fixed pressure and then raising the temperature), the  $\text{Fe}_3\text{S}$  stayed in the tetragonal structure (37), while the FeS transitioned from FeS III to IV phase at  $\sim 730$  K (38). Although our measurement temperature was only up to  $\sim 1023$  K, we observed clear temperature dependences that change with the pressure and S content. We should note that the estimated Martian core temperature was  $\sim 2000$  to  $2400$  K (39). If we assume that the thermal conductivity can be phenomenologically modeled as  $\Lambda(T) = aT^n$ , where  $a$  is a normalization constant, the exponent value  $n$  can be determined by the linear slope in the  $\ln\Lambda$ - $\ln T$  plot. For  $\text{Fe}_3\text{S}$ ,  $n = 0.25 (\pm 0.07)$  at  $15.4$  GPa and slightly decreases with pressure to  $n = 0.2 (\pm 0.04)$  at  $35.5$  GPa (Fig. 2A). With higher content of S impurity that results in

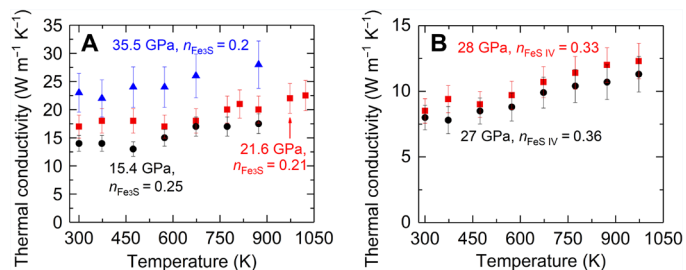


**Fig. 2. Temperature dependence of the thermal conductivity of Fe-S alloys at high pressures.** Assuming that the thermal conductivity scales with  $T^n$ , the  $n$  for (A)  $\text{Fe}_3\text{S}$  decreases from 0.25 ( $\pm 0.07$ ) at 15.4 GPa to 0.2 ( $\pm 0.04$ ) at 35.5 GPa. (B) The  $\text{FeS IV}$  phase (at  $T > 730$  K) has a larger temperature exponent  $n$  (0.33 at 28 GPa and 0.36 at 27 GPa) than that of  $\text{Fe}_3\text{S}$  (0.2 to 0.25) at relevant Martian core's pressures. Vertical bars represent analysis uncertainties of the data at  $\sim 10$  to 15%. The pressure uncertainty at high temperatures is typically less than 2 GPa. The uncertainty in the  $n$  values due to the pressure uncertainty does not influence our conclusion of a thermally conductive Martian core (see the main text).

stronger carrier scattering, the  $\text{FeS IV}$  phase has a stronger temperature dependence than the  $\text{Fe}_3\text{S}$  at similar pressures:  $n = 0.36$  ( $\pm 0.07$ ) at 27 GPa and  $n = 0.33$  ( $\pm 0.05$ ) at 28 GPa, respectively (Fig. 2B). Although the crystal structure of  $\text{Fe}_3\text{S}$  and  $\text{FeS}$  is different, our results suggest that at a given pressure, the higher content of impurity would have a stronger temperature dependence, which has also been reported in Fe-Si alloys (2, 36) (see Discussion).

## DISCUSSION

### Temperature dependence of thermal conductivity

The WF law relates the electronic thermal conductivity  $\Lambda_e$  of a material with its electrical resistivity  $\rho$  by  $\Lambda_e = L \times T/\rho$ , where  $L$  is the Lorenz number that may vary with pressure and temperature, and  $T$  is the absolute temperature. Typically, when the temperature is comparable or higher than the Debye temperature of the material, its electrical resistivity can be expressed approximately as  $\rho = \rho_0 + \alpha + \beta T$ , where  $\rho_0$  is the residual resistivity arisen from defect scattering,  $\alpha$  is a phenomenological constant associated with the shift in the resistivity due to temperature effect, and  $\beta$  is a temperature coefficient (40, 41). Therefore,  $\Lambda_e$  can be rewritten as  $\Lambda_e \sim L \times T/(\rho_0 + \alpha + \beta T)$ . Since our measurement temperature (300 to 1023 K) is higher than one-third of the Debye temperature of Fe-S alloys ( $\sim 400$  K) (42), the high contents of S impurity in Fe makes the sum of  $(\rho_0 + \alpha)$  larger than  $\beta T$  (41). The  $\Lambda_e$  of Fe-S alloys is thus expected to increase with increasing temperature. Furthermore, with increasing S content, the relative contribution of  $\beta T$  to the total electrical resistivity would be further reduced, leading to a stronger temperature dependence. On the other hand, for both  $\text{Fe}_3\text{S}$  and  $\text{FeS}$ , the temperature exponent  $n$  decreases with pressure, in line with the general trend observed for the  $\text{Fe}_{0.85}\text{Si}_{0.15}$  (2). This is presumably caused by the fact that pressure reduces the effective density of impurity in momentum space (less impurity scattering) and enhances the relative contribution of  $\beta T$ , leading to a weaker temperature dependence of thermal conductivity (40).

### Thermal conductivity profiles in Martian core and mantle

The recent geophysical observations by the InSight mission (21) suggest that the Martian core is larger than previously thought and confirm that, by contrast to the Earth, the Martian mantle is too thin

to allow a transition from ringwoodite to bridgmanite, i.e., ringwoodite is the major mineral in its deep mantle. The mean Martian core density derived from InSight observations spans from  $\sim 5.7$  to  $6.3 \text{ g cm}^{-3}$ , where a number of potential combinations of S, O, and H contents alloyed in an Fe-Ni core is discussed (21). Geochemically defensible amounts of these light elements with a mean core density  $> 6 \text{ g cm}^{-3}$  are at the upper end of such density range. With a lower bulk mantle FeO content, the InSight observations preliminarily suggests that the core is majorly composed of Fe-Ni along with  $\sim 10$  to 15 wt % S,  $< 5$  wt % O, and  $< 1$  wt % H and C (21). To understand the thermal evolution history of Mars and its early dynamo, we first model the thermal conductivity of the Martian core and mantle along an estimated Martian areotherm taken from (39) (an estimated present-day radial temperature profile within Mars), based on our present high  $P$ - $T$  thermal conductivity of solid Fe-S alloys and previous data for ringwoodite (25). Note that if the core temperature were as high as 3000 K early in Mars' history, then our modeled thermal conductivity of Martian core would be increased by only  $\sim 6\%$ , which is within our data uncertainty. In other words, the temporal changes in the Martian areotherm as it cools down since its early stage have minor effects on our modeled thermal conductivity and numerical simulations on its thermal evolution. For the solid  $\text{Fe}_3\text{S}$  and  $\text{FeS}$ , we assume their temperature dependences of thermal conductivity at Martian core  $P$ - $T$  conditions follow those shown in Fig. 2, i.e., scaling with  $T^{0.21}$  and  $T^{0.33}$ , respectively. The thermal conductivity of ringwoodite, on the other hand, is assumed to follow a  $T^{-0.5}$  dependence, typical of Fe-bearing minerals (31, 43–45). The modeled thermal conductivities of ringwoodite (blue curves), solid  $\text{Fe}_3\text{S}$  (black curve), and solid  $\text{FeS}$  (orange curve) along a Martian areotherm are plotted in Fig. 3.

Literature experimental investigations on the high  $P$ - $T$  electrical resistivity  $\rho$  of solid Fe-S alloys have been largely limited to  $\leq 10$  GPa (28–30). For instance,  $\rho$  of Fe-20 wt % S at 4.5 GPa was found to be  $\sim 400$  microhm cm up to  $\sim 1400$  K (28), and  $\rho$  of  $\text{FeS}$  at 5 GPa (30) and 8 GPa (28) remained at  $\sim 400$  and  $\sim 700$  microhm cm, respectively, up to  $\sim 1700$  K. Their corresponding thermal conductivities were then further inferred to be  $\sim 6$  to  $11 \text{ W m}^{-1} \text{ K}^{-1}$  via the WF law with an ideal Lorenz number. In addition, on the basis of high pressure but room temperature electrical resistivity measurements,  $\rho$  of solid Fe-14.2 wt % S at Martian core conditions was estimated to  $\sim 100$  microhm cm, suggesting a thermal conductivity of  $46 \text{ W m}^{-1} \text{ K}^{-1}$  at the Martian CMB and  $62 \text{ W m}^{-1} \text{ K}^{-1}$  at the center (46). Using first-principles calculations,  $\rho$  of liquid  $\text{Fe}_3\text{S}$  and  $\text{Fe}_7\text{S}$  were determined to stay at  $\sim 107$  and  $\sim 88$  microhm cm, respectively, throughout the Martian core conditions (27). Again, it is important to note that our present study represents the first direct high  $P$ - $T$  thermal conductivity measurements of solid Fe-S alloys that do not rely on the WF law and assumption of ideal Lorenz number. Our results for the thermal conductivities of solid Fe-S alloys (solid black and orange curves in Fig. 3) under similar  $P$ - $T$  conditions and S content are much higher than those inferred from high  $P$ - $T$  experimental electrical resistivity data (28), while only about half of those estimated from room temperature resistivity data (46) and calculated by first-principles (for liquid phase) (27). Table 1 summarizes thermal conductivity of Fe-S alloys at Martian CMB conditions. Here, we only include literature results available at CMB  $P$ - $T$  conditions with an S content similar to our present study, as the chemical composition could significantly influence the thermal conductivity of Fe alloys.



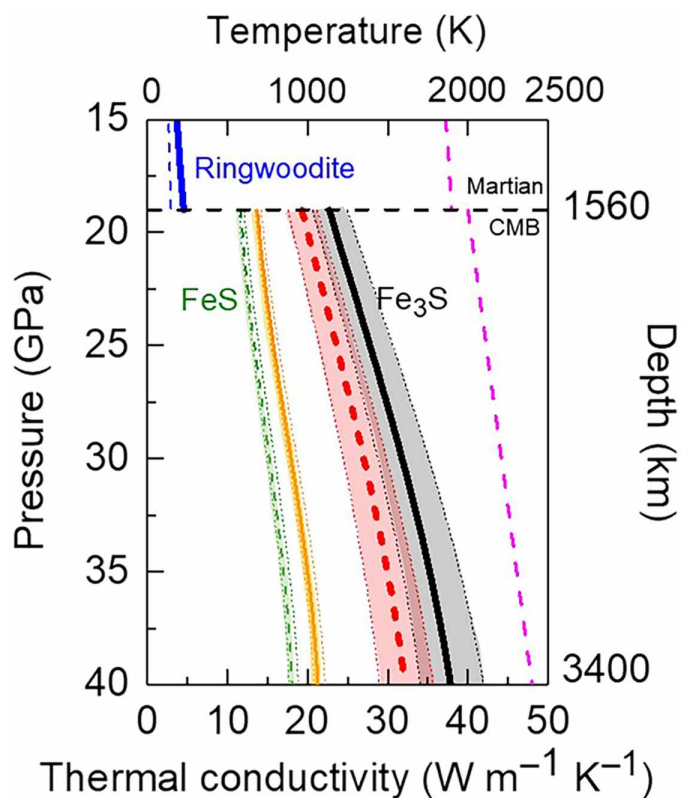


**Fig. 3. Modeled thermal conductivity profile in Martian mantle and core.** Assuming the Martian liquid core is majorly composed of  $\text{Fe}_3\text{S}$  (24), its thermal conductivity (red dashed curve) spans from  $\sim 19 \text{ W m}^{-1} \text{ K}^{-1}$  at the top to  $\sim 32 \text{ W m}^{-1} \text{ K}^{-1}$  at the center. The thermal conductivity of  $\text{FeS}$  in solid (orange curve) and liquid (green dashed curve) phases, respectively, are plotted for comparison. Note that the thermal conductivity of liquid  $\text{FeS}$  was estimated by a 15% reduction from that of the  $\text{FeS V}$  phase, which was assumed to have the same temperature dependence as  $\text{FeS IV}$  phase. The shaded areas represent the uncertainty ranges considering the small variation of the temperature exponent  $n$ . The solid and dashed blue curves are the thermal conductivity of ringwoodite with 0.11 wt % (dry) and 1.73 wt % (hydrous) water (25), respectively, along an estimated Martian mantle areotherm (magenta dashed curve with the temperature scale at the top axis) taken from (39). A  $\sim 4$ - to  $\sim 6$ -fold discontinuity in the thermal conductivity across the Martian CMB (liquid  $\text{Fe}_3\text{S}$  versus ringwoodite) is estimated.

Moreover, prior studies have suggested that the effect of melting would reduce the thermal conductivity of Fe and Fe alloys by  $\sim 20\%$  or less [see, e.g., (2) and references therein]. Assuming that S is the major light element with  $\sim 16 \text{ wt } \%$  ( $\sim 25 \text{ atomic } \%$ ) (24) in the Martian core and a 15% conductivity reduction upon melting, our present data suggest that the thermal conductivity of liquid  $\text{Fe}_3\text{S}$  (red dashed curve in Fig. 3) would be  $\sim 19 \text{ W m}^{-1} \text{ K}^{-1}$  at the top of the Martian core and that it increases by  $\sim 70\%$  to  $\sim 32 \text{ W m}^{-1} \text{ K}^{-1}$  at the center, leading to a much more thermally conductive Martian core than previously inferred. In addition, if the mineralogy of the Martian mantle is similar to that of the Earth's upper mantle, which is predominantly composed of olivine and its high-pressure polymorph ringwoodite, then the thermal conductivity of ringwoodite in dry phase at the bottom of the mantle would be  $\sim 4.5 \text{ W m}^{-1} \text{ K}^{-1}$  (blue solid curve in Fig. 3). Note that if the ringwoodite in the Martian mantle contains substantial amounts of water, its thermal conductivity would be

lower. For instance, the presence of 1.73 wt % water would lead to a conductivity of  $\sim 3 \text{ W m}^{-1} \text{ K}^{-1}$  at the bottom of the Martian mantle (see the blue dashed curve). Furthermore, if the ringwoodite in the Martian mantle contains more iron than that in the Earth, then its thermal conductivity would be even lower. Overall, a  $\sim 4$ - to  $\sim 6$ -fold thermal conductivity discontinuity is expected across the Martian CMB (liquid  $\text{Fe}_3\text{S}$  versus ringwoodite), which would suppress heat released from the core and promote thermal stratification. Such findings yield distinct behaviors concerning the  $Q_c$  (see geodynamic modeling below). In addition, our results for  $\text{Fe}_3\text{S}$  and  $\text{FeS}$  at Martian core's  $P$ - $T$  conditions provide a platform to model the thermal conductivity of the Fe-S alloys with different S contents, since under different model assumptions the not-well-constrained S content in the Martian core may vary over the range we explored ( $\sim 16$  to  $36 \text{ wt } \%$ ) during Mars history. If the Martian core also contains few amounts of other elements (e.g., O, H, C, etc.), then these impurities are expected to further slightly reduce the thermal conductivity of Martian core, while their exact effects require future experimental and computational studies.

### Implications for Martian thermal evolution and dynamo cessation

Dynamo operation and duration strongly depend on core thermal conductivity. Higher thermal conductivity promotes faster dynamo decay through ohmic dissipation, and in the absence of gravitational energy released from core crystallization, the dynamo may rapidly switch off. Recent simulations of Mars core-mantle coupled evolution (1) indicate that the cessation time of the Martian magnetic field (11–13) can be explained with a core thermal conductivity in the range of  $16$  to  $35 \text{ W m}^{-1} \text{ K}^{-1}$ , provided that the mantle reference viscosity,  $\eta_0$ , is between  $10^{19}$  and  $10^{21} \text{ Pa s}$ . Modeling details further show that the pressure dependence of mantle viscosity (with an activation volume fixed to  $6 \text{ cm}^3 \text{ mol}^{-1}$ ) requires a lower range of reference viscosity ( $10^{19}$  to  $10^{20} \text{ Pa s}$ ) and thermal conductivity ( $< 20 \text{ W m}^{-1} \text{ K}^{-1}$ ) to explain this cessation time.

Here, we investigate how the radial profile of the core thermal conductivity,  $\Lambda_c$  (red dashed curve in Fig. 3), affects Mars thermal evolution. For this, we performed simulations coupling parameterized models of core and mantle evolution following the method developed in (1) (also see Materials and Methods), with the exception that the thermal conductivity is now allowed to vary with depth. Figure 4 plots evolution of key parameters [(A) heat flow  $Q_c$ , (B) entropy arising from ohmic dissipation,  $E_j$ , (C) bottom radius of the thermally stratified layer,  $r_s$ , and (D) temperature at the CMB] for three different scenarios, including the reference case in (1) (green curves). Thermal stratification is a consequence of a sub-isentropic heat flow (i.e.,  $Q_c$  is lower than the heat flow along an isentropic temperature gradient,  $Q_a$ ) and results in higher core temperatures. All cases were performed with the “standard” configuration of (1), i.e., the mantle viscosity does not depend on pressure (activation volume is set to zero), and the mantle abundance in heat-producing elements is that of (47). In addition, the initial mantle temperature and temperature jump at the CMB were set to 2327 and 182 K, respectively, corresponding to the standard reference case in (1) and leading to an initial CMB temperature of 2509 K. Dynamo switches off when  $E_j$  is below a small value  $E_{j,\text{min}}$ , corresponding to the minimum ohmic dissipation needed to self-sustain feedbacks between magnetohydrodynamic processes. For Earth, and in the case of a poloidal field, this value was estimated to  $1.0 \text{ MW K}^{-1}$  (48), which we

**Table 1. Recent experimental and computational results of electrical resistivity  $\rho$  and thermal conductivity  $\Lambda$  of Fe-S alloys at Martian CMB conditions.** DTCM, direct thermal conductivity measurement; E, extrapolation; ERM, electrical resistivity measurement; C, calculation; NA, not applicable.

Composition	$\rho$ (microhm cm)	$\Lambda$ (W m <sup>-1</sup> K <sup>-1</sup> )	Method	Reference
Solid Fe-16 wt % S	NA	~22.7	DTCM + E	This study
Solid Fe-36 wt % S	NA	~13.7	DTCM + E	This study
Solid Fe-14.2 wt % S	~100	~46*	ERM + E	(46)
Liquid Fe-16.1 wt % S	~107	~43.3*	C	(27)
Liquid Fe-7.6 wt % S	~88	~52.7*	C	(27)

\*Thermal conductivity was inferred from electrical resistivity via WF law with ideal Lorenz number.

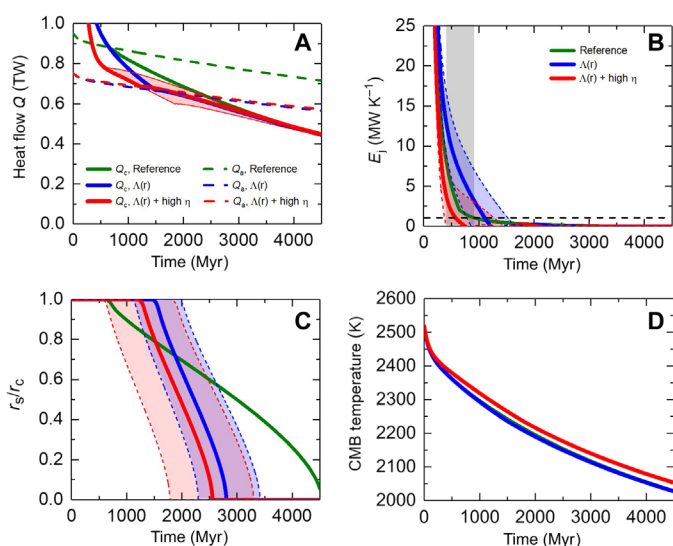


**Fig. 4. Thermal evolution scenarios of the Martian core.** Three scenarios are described in the text in detail. (A) Heat flow across the Martian CMB,  $Q_c$  (solid curves), versus isentropic heat flow,  $Q_a$  (dashed curves). TW, terawatt. (B) Entropy due to the Ohmic dissipation,  $E_j$ . The dynamo will stop as  $E_j < 1.0 \text{ MW K}^{-1}$  (horizontal dashed line), which occurs around the transition from super- to sub-isentropic heat flow, i.e.,  $Q_c$  being slightly higher or lower than  $Q_a$ . The gray zone indicates the range of cessation time of dynamo based on remnant crustal magnetism. (C) Ratio of the radius of the base of thermal stratification layer ( $r_s$ ) to the radius of the core ( $r_c$ ). Thermal stratification starts when  $Q_c$  becomes lower than  $Q_a$ . The shaded region in all the figures represents the uncertainty of each curve. (D) Temperature at the Martian CMB, where the green and blue curves are close to each other.

adopted in our estimation of the Martian dynamo cessation time. Greenwood *et al.* (1) pointed out that because  $E_{j,\min}$  is much smaller than the dissipation provided by secular cooling, its exact value does not substantially influence the dynamo cessation time. The condition  $E_j < 1.0 \text{ MW K}^{-1}$  occurs around the transition from super- to sub-isentropic heat flow (i.e.,  $Q_c$  being slightly higher or lower than  $Q_a$ ). For the reference case ( $\Lambda_c$  is a constant of  $24 \text{ W m}^{-1} \text{ K}^{-1}$  throughout the core and  $\eta_0 = 2.5 \times 10^{20} \text{ Pa s}$ ; green curves in Fig. 4), this happens ~0.9 Gyr, well within the estimated cessation range (11–13). For the depth-dependent profile of  $\Lambda_c$  based on our experimental data and still with  $\eta_0 = 2.5 \times 10^{20} \text{ Pa s}$ , dynamo cessation occurs later, ~1.1 Gyr (blue curves in Fig. 4). Within error bars (blue shaded area), however, the cessation time expected from our  $\Lambda_c$  profile agrees with the observed range. In addition, good agreement can

be obtained by assuming a slightly higher mantle viscosity (red curves in Fig. 4, the same  $\Lambda_c$  profile as the blue curves, but with  $\eta_0 = 3.5 \times 10^{20} \text{ Pa s}$ ). Thermal stratification starts when  $Q_c$  becomes lower than  $Q_a$ . Our calculations indicate that  $Q_a$  is lower with depth-increasing conductivity, which delays the onset of stratification. For the reference case, stratification starts ~0.3 Gyr before dynamo cessation, while it starts ~0.4 to 0.6 Gyr after dynamo cessation when the depth-dependent  $\Lambda_c$  is accounted for. Moreover, core thermal stratification is much faster with the depth-dependent  $\Lambda_c$ . For instance, the entire core is thermally stratified by 2.8 Gyr with our  $\Lambda_c$  profile and  $\eta_0 = 2.5 \times 10^{20} \text{ Pa s}$  (blue curve in Fig. 4C), compared to ~4.5 Gyr for the reference case (green curve). A possible explanation for this faster stratification is that, compared to the constant  $\Lambda_c$  case, because of the depth-increasing  $\Lambda_c$ , the increase in cooling rate of the convecting core is greater than that of the stable layer, meaning that the thermal stratification completes earlier.

One aspect that is not accounted for in our simulations is the presence of a layer of molten silicate rocks at the base of the mantle, as recently inferred by InSight seismic data (19, 20). This layer may result from the crystallization of Martian magma ocean and is possibly enriched in iron and heat-producing elements at the base of the mantle (49). Because it is partially molten and enriched in iron, one would further expect the thermal conductivity of this layer to be much lower than that of ringwoodite (blue curve in Fig. 3). In other words, the mantle basal layer may act as a thermal blanket, opposing core cooling and dynamo action. Combined with our present core thermal conductivity, this would, in turn, request a lower mantle viscosity to explain the observed dynamo cessation time. Future direct measurements and computational studies on the thermal conductivity of other Fe-S–light element systems under relevant  $P$ - $T$  conditions are required to better constrain the thermal evolution and energy budget of the Mars.

## MATERIALS AND METHODS

### Starting materials and sample preparation

The  $\text{Fe}_3\text{S}$  polycrystals were synthesized by a Kawai apparatus with a 5000-tonne press (run number 5K3187). The starting material is a powder mixture of Fe and S with an atomic ratio of 3:1. The sample was compressed to 22 GPa and first heated to  $1000^\circ\text{C}$ , followed by a cooling process from  $1000^\circ$  to  $855^\circ\text{C}$  for 9.5 hours and lastly kept at  $700^\circ\text{C}$  for 2 hours. The starting FeS troilite powder was extracted from the Cape York IIIAB iron meteorite, also known as the Innaanganeq meteorite, in the Geological Museum of the University of Copenhagen, Denmark. Troilite in iron meteorites is known to be very

chemically stoichiometric FeS, which is more suitable for the present study than commercial pyrrhotite samples ( $\text{Fe}_{1-X}\text{S}$ ) with iron deficiency ( $X = 0$  to 0.2). The chemical composition of  $\text{Fe}_3\text{S}$  and FeS was characterized to be  $\text{Fe}_{2.97}\text{S}$  (with a small amount of  $\text{Fe}_3\text{S}_2$ ) and  $\text{Fe}_{0.995}\text{S}$ , respectively, by electron probe microanalyzer in Academia Sinica.

To prepare samples for thermal conductivity measurements at high pressure and room temperature, each sample was firstly hand-polished down to  $\sim 10\ \mu\text{m}$  thick and then thermally evaporated with a 90-nm-thick Al film. The sample along with several ruby spheres was loaded into a symmetric DAC where a pair of 300- $\mu\text{m}$  culet anvils and a Re gasket were used. Because of its relatively low thermal conductivity at high pressures, silicone oil (Chemical Abstracts Service no. 63148-62-9 from Acros Organics) was loaded as the pressure transmitting medium, which remains in a reasonably well quasi-hydrostatic condition over the pressure range we studied ( $< 45\ \text{GPa}$ ). The pressure within the sample chamber of the DAC was monitored by fluorescence (50) and Raman of the ruby with a typical uncertainty of  $< 5\%$ .

In our high  $P$ - $T$  measurements, the  $\sim 10\text{-}\mu\text{m}$ -thick sample and ruby spheres were loaded into an EHDAC. Here, polycrystalline NaCl powder (thermally dried at  $\sim 120^\circ\text{C}$  for 1 hour before being loaded) was used as the pressure medium. The EHDAC provides a spatially homogeneous temperature distribution over the sample chamber. Since the pressure within the sample chamber may change upon heating, a gas membrane that enables in situ control on the pressure within the EHDAC was also used, allowing us to keep the pressure as close as possible (within  $\sim 1\ \text{GPa}$  variation range) to our target pressure. The combination of these techniques allows us to investigate the temperature dependence of thermal conductivity of  $\text{Fe}_3\text{S}$  and FeS at a given pressure up to  $\sim 1023\ \text{K}$ . Details of the EHDAC assemblage and pressure-temperature measurement, as well as the sample geometry and experimental setup, can be found in (43, 51). Note that as expected from previous reports, our measured ruby R1 fluorescence peak does become weak and broad at temperatures higher than  $\sim 700\ \text{K}$ . At a given high temperature, we determined the peak position with a typical wavelength uncertainty of  $\sim 0.05$  to  $0.2\ \text{nm}$ , which could translate a pressure uncertainty of  $\sim 0.1$  to  $0.6\ \text{GPa}$  using the temperature correction formula in (52). In addition, the uncertainty of temperature measurement using an R-type thermocouple is only about few Kelvin, which could induce an additional pressure uncertainty of  $\sim 0.05$  to  $0.1\ \text{GPa}$ . Thus, in our study, the overall pressure uncertainty at either room temperature or high temperature is typically less than  $2\ \text{GPa}$ . In our data analysis (Figs. 1 and 2 and fig. S2), we have already taken into account the effect of such pressure uncertainty.

### Thermal conductivity measurements

We used TDTR to measure the thermal conductivity of  $\text{Fe}_3\text{S}$  and FeS over a wide range of  $P$ - $T$  conditions presented in this work. TDTR is a widely used thermal metrology method that provides thermal conductivity measurements of various materials with high precision. In the past decade, it has also been successfully coupled with high  $P$ - $T$  techniques, see, e.g., (2, 31, 43, 53). In short, TDTR is an ultrafast optical pump-probe spectroscopy, which uses a split pump pulse to heat up the Al film coated on the sample and a split probe pulse to detect the heat diffusion dynamics through the sample. By comparing the temporal evolution of the Al's reflectivity change with numerical calculations based on a bidirectional thermal model,

the thermal conductivity of the sample of interest is determined. More details of the principle, experimental setup, and data analysis of the TDTR are described in literatures, e.g., (2, 51, 53–55) and references therein.

Figure S1 shows a set of representative TDTR spectrum for  $\text{Fe}_3\text{S}$  at 40.5 GPa and room temperature along with data fitting by the thermal model calculations. In the thermal model, the volumetric heat capacity of the sample of interest (Fe-S alloys) is an important parameter. At ambient conditions, the volumetric heat capacity of FeS is  $2.78\ \text{J cm}^{-3}\ \text{K}^{-1}$  taken from (56) while that of  $\text{Fe}_3\text{S}$  is estimated to be  $3.16\ \text{J cm}^{-3}\ \text{K}^{-1}$  by linear interpolation between pure Fe ( $3.54\ \text{J cm}^{-3}\ \text{K}^{-1}$ ) and FeS. The heat capacity of both FeS and  $\text{Fe}_3\text{S}$  at high  $P$ - $T$  conditions is not known and thus assumed to be a constant as their ambient values. We note that the uncertainty in our data majorly arises from the analysis uncertainty rather than the measurement uncertainty. On the basis of the method (57, 58) described in figs. S1 and S2, the uncertainties in all the parameters in our thermal model calculations would translate  $< 10\%$  error in the derived thermal conductivity of Fe-S alloys before 20 GPa and  $\sim 10$  to 17% error at 20 to 40 GPa.

### Modeling of core evolution

To investigate the evolution of the Martian core, including the growth of a stable layer, and to estimate the cessation time of Martian dynamo, we used the approach in (1), which is coupling models of parameterized convection for the core and for the mantle. For the mantle, this approach uses a parameterization based on stagnant lid thermal convection (59, 60) with a simplified lithosphere. The mantle is heated both from below (heat extracted from the core) and from within (radiogenic heating due to the decay of U, Th, and K). Concentration in heat-producing elements is taken from the compositional model of (47). The convective interior is assumed isothermal, and temperature increases linearly with depth within thermal boundary layers. The crust thickness is considered as constant over time, and melting and crust growth are neglected. The thickness of the stagnant lid (modeling the lithosphere) is set to 300 km. Greenwood *et al.* (1) showed that the thickness of the stagnant lid does not have a strong impact on the evolution of the mantle convective interior and of the core. Mantle viscosity depends on temperature following an Arrhenius law with activation energy fixed to  $300\ \text{kJ mol}^{-1}$  and is specified (reference viscosity  $\eta_0$ ) at a temperature of 1600 K. Viscosity is further allowed to increase with temperature, but, for simplicity, here is neglected this dependence (activation volume  $V_a$  is set to 0). The time for dynamo's cessation strongly depends on  $\eta_0$  and, to a lesser extent, on activation volume (1). For core thermal conductivity in the range of  $16$  to  $35\ \text{W m}^{-1}\ \text{K}^{-1}$ , calculated cessation time agrees with that estimated for Martian dynamo with viscosity in the range of  $10^{20}$  to  $10^{21}\ \text{Pa s}$ . Accounting for viscosity pressure dependence ( $V_a = 6\ \text{cm}^3\ \text{mol}^{-1}$ ) reduces this range by one order of magnitude. In calculations, we tested values of the reference viscosity,  $\eta_0 = 2.5 \times 10^{20}\ \text{Pa s}$  and  $\eta_0 = 3.5 \times 10^{20}\ \text{Pa s}$ .

The core is initially well mixed with an adiabatic temperature profile and is animated with convection. The core is initially assumed super-heated compared to the mantle with a temperature difference  $dT$ , which we fixed to 182 K, based on the standard model from (1), and the temperature at the CMB is readjusted according to this treatment. The heat flow at CMB,  $Q_c$ , is calculated from scaling relationships built for mantle convection (60) and is further depending on the temperature at the CMB,  $T_{\text{CMB}}$ , which is determined



from the core evolution. As  $Q_c$  becomes lower than the heat flow calculated along an isentropic temperature profile,  $Q_a$ , a stable conductive layer starts to grow, and core convection is confined beneath this layer. The evolution of the stable layer follows the treatment in (61). The ohmic dissipation related to magnetic field is measured with the entropy balance  $E_j$  between the entropies originating from secular cooling and thermal conduction,  $E_s$  and  $E_k$ , which are calculated following (61). Because  $E_k$  is proportional to the core thermal conductivity,  $\Lambda_c$ , larger conductivity leads to larger  $E_k$  and thus lower  $E_j$ . In other words, dynamo action is reduced with increasing  $\Lambda_c$  and may stop if conduction is too large.

## Supplementary Materials

This PDF file includes:

Figs. S1 and S2

Table S1

## REFERENCES AND NOTES

1. S. Greenwood, C. J. Davies, A. Pommier, Influence of thermal stratification on the structure and evolution of the martian core. *Geophys. Res. Lett.* **48**, e2021GL095198 (2021).
2. W.-P. Hsieh, A. F. Goncharov, S. Labrosse, N. Holtgrewe, S. S. Lobanov, I. Chuvashova, F. Deschamps, J.-F. Lin, Low thermal conductivity of iron-silicon alloys at Earth's core conditions with implications for the geodynamo. *Nat. Commun.* **11**, 3332 (2020).
3. K. Hirose, S. Labrosse, J. Hernlund, Composition and state of the core. *Annu. Rev. Earth Planet. Sci.* **41**, 657–691 (2013).
4. J.-P. Williams, F. Nimmo, Thermal evolution of the Martian core: Implications for an early dynamo. *Geology* **32**, 97–100 (2004).
5. C. J. Davies, A. Pommier, Iron snow in the Martian core? *Earth Planet. Sci. Lett.* **481**, 189–200 (2018).
6. B. A. Buffett, The thermal state of earth's core. *Science* **299**, 1675–1677 (2003).
7. S. Labrosse, Thermal and magnetic evolution of the Earth's core. *Phys. Earth Planet. Inter.* **140**, 127–143 (2003).
8. J. Badro, J. Siebert, F. Nimmo, An early geodynamo driven by exsolution of mantle components from Earth's core. *Nature* **536**, 326–328 (2016).
9. J. G. O'Rourke, D. J. Stevenson, Powering Earth's dynamo with magnesium precipitation from the core. *Nature* **529**, 387–389 (2016).
10. S. Yokoo, K. Hirose, S. Tagawa, G. Morard, Y. Ohishi, Stratification in planetary cores by liquid immiscibility in Fe-S-H. *Nat. Commun.* **13**, 644 (2022).
11. M. H. Acuña, J. E. P. Connerney, N. F. Ness, R. P. Lin, D. Mitchell, C. W. Carlson, J. McFadden, K. A. Anderson, H. Rème, C. Mazelle, D. Vignes, P. Wasilewski, P. Cloutier, Global distribution of crustal magnetization discovered by the Mars Global Surveyor MAG/ER experiment. *Science* **284**, 790–793 (1999).
12. B. Langlais, E. Thébaud, A. Houliéz, M. E. Purucker, R. J. Lillis, A new model of the crustal magnetic field of Mars using MGS and MAVEN. *J. Geophys. Res. Planets.* **124**, 1542–1569 (2019).
13. A. Mittelholz, C. L. Johnson, J. M. Feinberg, B. Langlais, R. J. Phillips, Timing of the martian dynamo: New constraints for a core field 4.5 and 3.7 Ga ago. *Sci. Adv.* **6**, eaba0513 (2020).
14. S. M. Tikoo, A. J. Evans, Dynamos in the inner solar system. *Annu. Rev. Earth Planet. Sci.* **50**, 99–122 (2022).
15. R. K. Bono, J. A. Tarduno, F. Nimmo, R. D. Cottrell, Young inner core inferred from Ediacaran ultra-low geomagnetic field intensity. *Nat. Geosci.* **12**, 143–147 (2019).
16. D. J. Hemingway, P. Driscoll, History and future of the martian dynamo and implications of a hypothetical solid inner core. *J. Geophys. Res. Planets.* **126**, e2020JE006663 (2021).
17. M. Dumbergy, A. Rivoldini, Mercury's inner core size and core-crystallization regime. *Icarus* **248**, 254–268 (2015).
18. I. Wardinski, H. Amit, B. Langlais, E. Thebaud, The internal structure of mercury's core inferred from magnetic observations. *J. Geophys. Res. Planets.* **126**, e2020JE006792 (2021).
19. A. Khan, D. Huang, C. Durán, P. A. Sossi, D. Giardini, M. Murakami, Evidence for a liquid silicate layer atop the Martian core. *Nature* **622**, 718–723 (2023).
20. H. Samuel, M. Drilleau, A. Rivoldini, Z. Xu, Q. Huang, R. F. Garcia, V. Lekic, J. C. E. Irving, J. Badro, P. H. Lognonné, J. A. D. Connolly, T. Kawamura, T. Gudkova, W. B. Banerdt, Geophysical evidence for an enriched molten silicate layer above Mars's core. *Nature* **622**, 712–717 (2023).
21. S. C. Stähler, A. Khan, W. Bruce Banerdt, P. Lognonné, D. Giardini, S. Ceylan, M. Drilleau, A. Cecilia Duran, R. F. Garcia, Q. Huang, D. Kim, V. Lekic, H. Samuel, M. Schimmel, N. Schmerr, D. Sollberger, É. Stutzmann, Z. Xu, D. Antonangeli, C. Charalambous, P. M. Davis, J. C. E. Irving, T. Kawamura, M. Knapmeyer, R. Maguire, A. G. Marusiak, M. P. Panning, C. Perrin, A. C. Plesa, A. Rivoldini, C. Schmelzbach, G. Zenhäusern, É. Beucler, J. Clinton, N. Dahmen, M. van Driel, T. Gudkova, A. Horleston, W. Thomas Pike, M. Plasman, S. E. Smrekar, Seismic detection of the martian core. *Science* **373**, 443–448 (2021).
22. T. Yoshizaki, W. F. McDonough, The composition of Mars. *Geochim. Cosmochim. Acta* **273**, 137–162 (2020).
23. G. J. Taylor, The bulk composition of Mars. *Geochemistry* **73**, 401–420 (2013).
24. G. Helffrich, Mars core structure—concise review and anticipated insights from insight. *Prog. Earth Planet. Sci.* **4**, 24 (2017).
25. E. Marzotto, W. P. Hsieh, T. Ishii, K. H. Chao, G. J. Golabek, M. Thielmann, E. Ohtani, Effect of water on lattice thermal conductivity of ringwoodite and its implications for the thermal evolution of descending slabs. *Geophys. Res. Lett.* **47**, e2020GL087607 (2020).
26. M. Berrada, R. A. Secco, Review of electrical resistivity measurements and calculations of Fe and Fe-alloys relating to planetary cores. *Front. Earth Sci.* **9**, 732289 (2021).
27. F. Wagle, G. Steinle-neumann, N. De Koker, Resistivity saturation in liquid iron-light-element alloys at conditions of planetary cores from first principles computations. *C. R. Geosci.* **351**, 154–162 (2019).
28. A. Pommier, Influence of sulfur on the electrical resistivity of a crystallizing core in small terrestrial bodies. *Earth Planet. Sci. Lett.* **496**, 37–46 (2018).
29. G. Manthilake, J. Chantel, J. Monteux, D. Andrault, M. A. Bouhifd, N. Bolfan Casanova, E. Boulard, N. Guignot, A. King, J. P. Itie, Thermal conductivity of FeS and its implications for Mercury's long-sustaining magnetic field. *J. Geophys. Res. Planets.* **124**, 2359–2368 (2019).
30. J. A. H. Littleton, R. A. Secco, W. Yong, Electrical resistivity of FeS at high pressures and temperatures: Implications of thermal transport in the core of ganymede. *J. Geophys. Res. Planets.* **126**, e2020JE006793 (2021).
31. W.-P. Hsieh, F. Deschamps, T. Okuchi, J.-F. Lin, Effects of iron on the lattice thermal conductivity of Earth's deep mantle and implications for mantle dynamics. *Proc. Natl. Acad. Sci. U.S.A.* **115**, 4099–4104 (2018).
32. W.-P. Hsieh, F. Deschamps, T. Okuchi, J.-F. Lin, Reduced lattice thermal conductivity of Fe-bearing bridgmanite in Earth's deep mantle. *J. Geophys. Res. Solid Earth.* **122**, 4900–4917 (2017).
33. H. Gomi, K. Ohta, K. Hirose, S. Labrosse, R. Caracas, M. J. Verstraete, J. W. Hernlund, The high conductivity of iron and thermal evolution of the Earth's core. *Phys. Earth Planet. Inter.* **224**, 88–103 (2013).
34. H. Gomi, K. Hirose, H. Akai, Y. Fei, Electrical resistivity of substitutionally disordered hcp Fe–Si and Fe–Ni alloys: Chemically-induced resistivity saturation in the Earth's core. *Earth Planet. Sci. Lett.* **451**, 51–61 (2016).
35. C. T. Seagle, E. Cottrell, Y. Fei, D. R. Hummer, V. B. Prakapenka, Electrical and thermal transport properties of iron and iron-silicon alloy at high pressure. *Geophys. Res. Lett.* **40**, 5377–5381 (2013).
36. M. Pozzo, C. J. Davies, D. Alfè, Towards reconciling experimental and computational determinations of Earth's core thermal conductivity. *Earth Planet. Sci. Lett.* **584**, 117466 (2022).
37. S. Thompson, T. Komabayashi, H. Breton, S. Suehiro, K. Glazyrin, A. Pakhomova, Y. Ohishi, Compression experiments to 126 GPa and 2500 K and thermal equation of state of Fe3S: Implications for sulphur in the Earth's core. *Earth Planet. Sci. Lett.* **534**, 116080 (2020).
38. S. Urakawa, K. Someya, H. Terasaki, T. Katsura, S. Yokoshi, K. I. Funakoshi, W. Utsumi, Y. Katayama, Y. I. Sueda, T. Irifune, Phase relationships and equations of state for FeS at high pressures and temperatures and implications for the internal structure of Mars. *Phys. Earth Planet. Inter.* **143–144**, 469–479 (2004).
39. Y. Fei, C. Bertka, The Interior of Mars. *Science* **308**, 1120–1121 (2005).
40. W. S. Williams, The thermal conductivity of metallic ceramics. *JOM* **50**, 62–66 (1998).
41. Q. Zheng, A. B. Mei, M. Tuteja, D. G. Sangiovanni, L. Hultman, I. Petrov, J. E. Greene, D. G. Cahill, Phonon and electron contributions to the thermal conductivity of VN<sub>x</sub> epitaxial layers. *Phys. Rev. Mater.* **1**, 065002 (2017).
42. F. Grønvdal, S. Stølen, A. K. Labban, E. F. Westrum Jr., Thermodynamics of iron sulfides I. Heat capacity and thermodynamic properties of Fe<sub>9</sub>S<sub>10</sub> at temperatures from 5 K to 740 K. *J. Chem. Thermodyn.* **23**, 261–272 (1991).
43. W.-P. Hsieh, E. Marzotto, T. Ishii, L. Dubrovinsky, A. A. Aslandukova, G. Criniti, Y. Tsao, C. Lin, J. Tsuchiya, E. Ohtani, Low thermal conductivity of hydrous phase D leads to a self-preservation effect within a subducting slab. *J. Geophys. Res. Solid Earth* **127**, e2022JB024556 (2022).
44. Y. Xu, T. J. Shankland, S. Linhardt, D. C. Rubie, F. Langenhorst, K. Klasinski, Thermal diffusivity and conductivity of olivine, wadsleyite and ringwoodite to 20 GPa and 1373 K. *Phys. Earth Planet. Inter.* **143–144**, 321–336 (2004).
45. Y. Zhang, T. Yoshino, A. Yoneda, M. Osako, Effect of iron content on thermal conductivity of olivine with implications for cooling history of rocky planets. *Earth Planet. Sci. Lett.* **519**, 109–119 (2019).
46. S. Suehiro, K. Ohta, K. Hirose, G. Morard, Y. Ohishi, The influence of sulfur on the electrical resistivity of hcp iron: Implications for the core conductivity of Mars and Earth. *Geophys. Res. Lett.* **44**, 8254–8259 (2017).

47. H. Wänke, G. Dreibus, Chemistry and accretion history of Mars. *Phil. Trans. R. Soc. Lond. A* **349**, 285–293 (1994).
48. A. Jackson, P. W. Livermore, G. Ierley, On Ohmic heating in the Earth's core II: Poloidal magnetic fields obeying Taylor's constraint. *Phys. Earth Planet. Inter.* **187**, 322–327 (2011).
49. H. Samuel, M. D. Ballmer, S. Padovan, N. Tosi, A. Rivoldini, A.-C. Plesa, The thermo-chemical evolution of Mars with a strongly stratified mantle. *J. Geophys. Res. Planets* **126**, e2020JE006613 (2021).
50. A. Dewaele, P. Loubeyre, M. Mezouar, Equations of state of six metals above 94 GPa. *Phys. Rev. B* **70**, 094112 (2004).
51. W.-P. Hsieh, High-pressure thermal conductivity and compressional velocity of NaCl in B1 and B2 phase. *Sci. Rep.* **11**, 21321 (2021).
52. F. Datchi, A. Dewaele, P. Loubeyre, R. Letoulec, Y. Le Godec, B. Canny, Optical pressure sensors for high-pressure-high-temperature studies in a diamond anvil cell. *High Press. Res.* **27**, 447–463 (2007).
53. W.-P. Hsieh, B. Chen, J. Li, P. Keblinski, D. G. Cahill, Pressure tuning of the thermal conductivity of the layered muscovite crystal. *Phys. Rev. B* **80**, 180302(R) (2009).
54. K. Kang, Y. K. Koh, C. Chiritescu, X. Zheng, D. G. Cahill, Two-tint pump-probe measurements using a femtosecond laser oscillator and sharp-edged optical filters. *Rev. Sci. Instrum.* **79**, 114901 (2008).
55. D. G. Cahill, Analysis of heat flow in layered structures for time-domain thermoreflectance. *Rev. Sci. Instrum.* **75**, 5119–5122 (2004).
56. F. Grønbold, E. F. Westrum, C. Chou, Heat capacities and thermodynamic properties of the pyrrhotites FeS and Fe<sub>0.877</sub>S from 5 to 350°K. *J. Chem. Phys.* **30**, 528–531 (1959).
57. D. G. Cahill, F. Watanabe, Thermal conductivity of isotopically pure and Ge-doped Si epitaxial layers from 300 to 550 K. *Phys. Rev. B* **70**, 235322 (2004).
58. X. Zheng, D. G. Cahill, P. Krasnochtchekov, R. S. Averback, J.-C. Zhao, High-throughput thermal conductivity measurements of nickel solid solutions and the applicability of the Wiedemann-Franz law. *Acta Mater.* **55**, 5177–5185 (2007).
59. D. Breuer, T. Spohn, Viscosity of the Martian mantle and its initial temperature: Constraints from crust formation history and the evolution of the magnetic field. *Planet. Space Sci.* **54**, 153–169 (2006).
60. M. Thiriet, D. Breuer, C. Michaut, A.-C. Plesa, Scaling laws of convection for cooling planets in a stagnant lid regime. *Phys. Earth Planet. Inter.* **286**, 138–153 (2019).
61. S. Greenwood, C. J. Davies, J. E. Mound, On the evolution of thermally stratified layers at the top of Earth's core. *Phys. Earth Planet. Inter.* **318**, 106763 (2021).

**Acknowledgments:** The troilite sample was provided by J. Connelly at Centre for Star and Planet Formation, GLOBE Institute, University of Copenhagen. The Fe<sub>3</sub>S samples were synthesized using joint-use facilities of the Institute for Planetary Materials, Okayama University. We are very grateful to C. J. Davies at University of Leeds, UK, for performing numerical simulations. We also thank Y. Iizuka at Academia Sinica for help with the EPMA analysis. **Funding:** This work was supported by Academia Sinica grant AS-IA-111-M02 (W.P.H.), National Science and Technology Council of Taiwan, Republic of China grant 110-2628-M-001-001-MY3 (W.P.H.), Foundation for the Advancement of Outstanding Scholarship, Taiwan (W.P.H.), and Solar System Workings (SSW) Program of the NASA, USA, grant number 80NSSC23K1274 (J.-F.L.). **Author contributions:** Conceptualization: W.P.H., F.D., and J.-F.L. Methodology: W.P.H. Source: T.Y. Investigation: W.P.H. and Y.-C.T. Supervision: W.P.H. and F.D. Writing—original draft: W.P.H. and F.D. Writing—review and editing: W.P.H., F.D., Y.-C.T., T.Y., and J.-F.L. **Competing interests:** The authors declare that they have no competing interests. **Data and materials availability:** All data needed to evaluate the conclusions in the paper are present in the paper and/or the Supplementary Materials. All experimental data are available in. <https://doi.org/10.5281/zenodo.10457090>.

Submitted 2 August 2023  
Accepted 15 February 2024  
Published 20 March 2024  
10.1126/sciadv.adk1087